Materials LAB

RESEARCH ARTICLE

Materials Lab 2026, 5, 260112

Impact of a-site cation size: structural evolution from brownmillerite to cubic phases in $Ca_2FeCoO_{6-\delta}$, $CaSrFeCoO_{6-\delta}$, and $Ca_{2/3}Sr_{2/3}Ba_{2/3}FeCoO_{6-\delta}$

Alexa D. Azure[1], Dominique Miner[1], Kadin Eagle[1] and Ram Krishna Hona[2*]

The synthesis and structural characterization of a novel oxygen-deficient perovskite, $Ca_{2/3}Sr_{2/3}Ba_{2/3}FeCoO_{6-\delta}$ (CSBFC), were successfully achieved using solid-state reactions under identical conditions as its previously reported counterparts, $Ca_2FeCoO_{6-\delta}$ and $CaSrFeCoO_{6-\delta}$. While $Ca_2FeCoO_{6-\delta}$ exhibits a brownmillerite-type orthorhombic structure with a *Pbcm* space group, and $CaSrFeCoO_{6-\delta}$ crystallizes in the orthorhombic *Ibm*2 space group, the introduction of Ba to achieve a mixed A-site cation composition (Ca, Sr, Ba) induces a transformation to a cubic structure with a *Pm*-3*m* space group. This structural evolution highlights the critical role of A-site cation size in modulating vacancy ordering. A systematic correlation was observed between the increasing average ionic radius of the A-site cations and the degree of vacancy disorder, with the sequence: $Ca_2FeCoO_{6-\delta}$ (2.68 Å) > $CaSrFeCoO_{6-\delta}$ (2.78 Å) > CSBFC (2.941 Å). As the A-site cation size increases, the vacancy ordering diminishes, with $Ca_2FeCoO_{6-\delta}$ being the most ordered and CSBFC the least. The cubic CSBFC phase exhibits the highest electrical conductivity, which can be attributed to its enhanced structural symmetry and increased oxygen-vacancy disorder, facilitating improved charge transport. These findings highlight the structural flexibility and tunability of oxygen-deficient perovskites through A-site cation engineering, offering promising implications for applications in catalysis and solid oxide fuel cells.

Oxygen-deficient perovskite oxides have garnered significant attention in recent years due to their unique structural flexibility and promising applications in catalysis, solid oxide fuel cells, and other energy-related technologies.[1, 2] These materials are characterized by their ability to accommodate oxygen vacancies, which can dramatically influence their electrical, magnetic, and catalytic properties. A crucial factor in controlling these vacancies and, consequently, the material's properties, is the selection of A-site cations.[3] The average ionic radius of the A-site cation plays a pivotal role in dictating the structural framework and vacancy ordering of perovskite compounds.

Brownmillerite-type oxides, such as $Ca_2FeCoO_{6-\delta}$, are well-documented for their orthorhombic structures (*Pbcm* space group) with ordered oxygen vacancies along specific crystallographic planes.[4] Substitution of the A-site cation with elements of varying ionic radii, such as Sr, leads to structural transformations. For example, $CaSrFeCoO_{6-\delta}$ exhibits an orthorhombic structure with a different space group (*Ibm*2) due to the changes in lattice parameters and vacancy arrangements driven by the increased A-site ionic radius. These modifications underscore the impact of A-site cation size on the overall structure and properties of perovskite materials.

In this study, we synthesized a novel oxygen-deficient perovskite, $Ca_{2/3}Sr_{2/3}Ba_{2/3}FeCoO_{6-\delta}$ (CSBFC), to further investigate the influence of mixed A-site cation compositions on structural transitions and vacancy ordering. By introducing Ba into the A-site composition, achieving an average cationic radius larger than that of both Ca and Sr, we observed a significant structural transformation from an orthorhombic to a cubic phase (*Pm*-3*m* space group). The systematic increase in the average ionic radius from $Ca_2FeCoO_{6-\delta}$ (2.68 Å) to $CaSrFeCoO_{6-\delta}$ (2.78 Å), and finally to CSBFC (2.941 Å), correlates with a progressive reduction in vacancy ordering. This transition highlights a direct relationship between A-site cation size and the degree of vacancy disorder, offering a new avenue for tailoring the structural and functional properties of perovskite oxides.

Experimental

Sample of $Ca_{2/3}Sr_{2/3}Ba_{2/3}FeCoO_{6-\delta}$ was prepared by conventional solid-state synthesis method. The powders of the precursor compounds $CaCO_3$ (Alfa Aesar, 99.95%), $SrCO_3$ (Alfa Aesar, 99.95%), $BaCO_3$ (Alfa Aesar, 99.95%), Fe_2O_3 (Alfa Aesar, 99.998) and Co_3O_4 (Alfa Aesar, 99.7%), were mixed and ground together using an agate mortar and pestle, pressed into a pellet, and heated at 1000 °C for 24 h in air. Then the samples were reground and re-fired at 1200 °C for 24 h in the same environments, followed by slow cooling. The heating and cooling rates were 100 °C/h in each time of firing. The

[1] *Engineering Department, United Tribes Technical College, Bismarck, ND 58504*

[2] *Environmental Science Department, United Tribes Technical College, Bismarck, ND 58504*

* Corresponding author, E-mail: rhona@uttc.edu, Phone: (701) 221-1329

Received 25 June 2026; Accepted 25 July 2026; Published online 7 August 2026

© 2026 The Author(s). *Materials Lab* published by Lab Academic Press

DOI: 10.54227/mlab.20260112

phase purity and structure of the polycrystalline samples were determined by powder X-ray diffraction (XRD) at room temperature using Bruker D2 Phaser diffractometer with Cu Kα1 radiation (λ = 1.54056 Å). The GSAS software[5] and EXPEGUI interface[6] were used for Rietveld refinements. Microstructures of the samples were studied using high resolution field-emission scanning electron microscopy (SEM). The electrical properties were investigated by direct-current (dc) measurements on as-prepared pellets that had been sintered at 1200 °C. The 4-probe dc measurements were performed in the temperature range of 25-800ºC by applying a constant voltage of 10 mV and collecting the output current. The rate of heating for conductivity measurements was 3 °C/min. Iodometric titrations were performed by dissolving about 50 mg of the sample and excess KI (~2 g) in 100 mL of 1M HCl. A total of 5 mL of the solution was then pipetted out, and the iodine that had been generated in the solution was titrated against 0.025 M $Na_2S_2O_3$. Near the end point of the titration, 0.2mL of a starch solution was added to act as an indicator. All steps were performed under an argon atmosphere.[7]

Results and discussions

Structural analysis

The crystal structures of the synthesized compounds were determined using Rietveld refinement of Powder X-ray Diffraction (XRD) data. The novel compound, $Ca_{2/3}Sr_{2/3}Ba_{2/3}FeCoO_{6-\delta}$ (CSBFC), was identified to crystallize in a cubic structure with the *Pm*-3*m* space group, as shown by its Rietveld refinement profile (Fig. 1c). In the cubic structure of oxygen-deficient perovskites (ODPs) like CSBFC, oxygen vacancies are distributed randomly, yet the structure is stabilized by corner-sharing FeO_6 octahedra similar to those found in simple cubic perovskites. The refined structural parameters of CSBFC are summarized in Table 1.

For comparison, the previously reported $Ca_2FeCoO_{6-\delta}$ and $CaSrFeCoO_{6-\delta}$ are also included in this study. The refined structural parameters of $Ca_2FeCoO_{6-\delta}$ and $CaSrFeCoO_{6-\delta}$ are summarized in Table 2 and 3, respectively. $Ca_2FeCoO_{6-\delta}$ adopts a brownmillerite-type orthorhombic structure with the *Pbcm* space group, which is characterized by alternating layers of FeO_6 octahedra and FeO_4 tetrahedra.[4] The Rietveld refinement profile and the corresponding crystallographic structure of $Ca_2FeCoO_{6-\delta}$ are depicted in Fig. 1a and 2a. When the Ca in $Ca_2FeCoO_{6-\delta}$ is partially substituted by Sr, the resulting compound, $CaSrFeCoO_{6-\delta}$, transforms into another orthorhombic structure[4] but with a different space group, *Ibm*2, as evidenced by its Rietveld refinement shown in Fig. 1b. The crystallographic structure of $CaSrFeCoO_{6-\delta}$ is shown in Fig. 2b. This transformation highlights the significant influence of A-site cation substitution on crystal symmetry and the ordering of vacancies.

Brownmillerite structures with *Pbcm* and *Ibm*2 space groups are known for their intricate arrangements of FeO_6 octahedra and FeO_4 tetrahedra. In these structures, octahedra within the same layer are corner-sharing, while they interact with tetrahedra in adjacent layers. However, distinguishing between *Pbcm* and *Ibm*2 structures can be challenging due to their similar lattice parameters. Figure (1a) illustrates the crystal structure of the orthorhombic *Pbcm* brownmillerite phase. The green polyhedra represent BO_6 octahedra, which form continuous layers by sharing their corners. Between these octahedral layers are BO_4 tetrahedra (shown in blue and red), which are formed because of the ordered removal of oxygen atoms from the parent perovskite structure. The oxygen vacancies are confined to these tetrahedral layers, converting some BO_6 octahedra into BO_4 tetrahedra. The tetrahedra are connected into zigzag chains, and neighboring chains alternate in orientation (left- and right-handed), which is the characteristic feature of the *Pbcm* space group. This alternating ar-

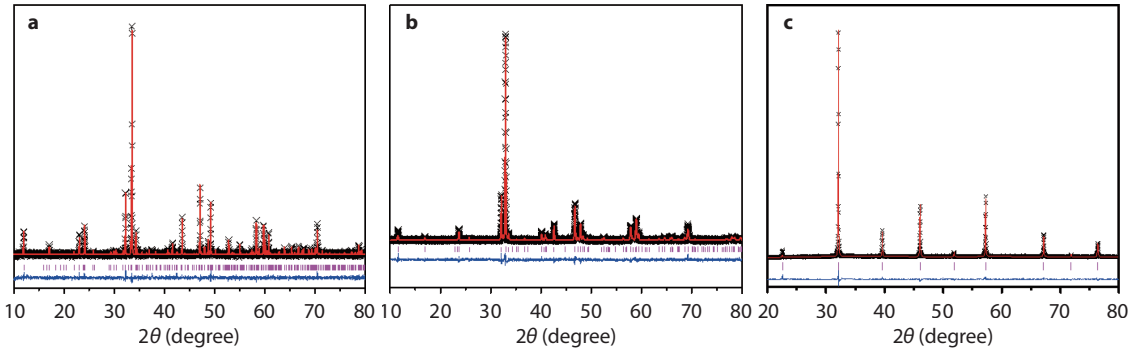


Fig. 1 Rietveld refined XRD data (profile) of **a** $Ca_2FeCoO_{6-\delta}$, **b** $CaSrFeCoO_{6-\delta}$, and c) $Ca_{2/3}Sr_{2/3}Ba_{2/3}FeCoO_{6-\delta}$.

Table 1. Cell parameters of $Ca_{2/3}Sr_{2/3}Ba_{2/3}FeCoO_{6-\delta}$ using powder X-ray diffraction: Cubic with *Pm*-3*m* space group.

A (Å)		V (Å^3)		alpha, beta, gamma		χ^2
3.94093(17)		61.206(8)		90°		1.99
element	x	y	z	Uiso	occupancy	multiplicity
O1	0	0.5	0.5	0.0671(6)	0.90	3
Fe1	0.5	0.5	0.5	0.0311(5)	0.5	1
Co1	0.5	0.5	0.5	0.0311(5)	0.5	1
Ba1	0	0	0	0.0107(8)	0.33	1
Sr1	0	0	0	0.0107(8)	0.33	1
Ca1	0	0	0	0.0107(8)	0.33	1

DOI: 10.54227/mlab.20260112

Table 2. Refined structural parameters of $Ca_2FeCoO_{6-\delta}$ using powder X-ray diffraction.

Space group: *Pbcm*						
a = 5.36854(3) Å, b = 11.1062(8) Å, c = 14.8079(8) Å, R_p = 0.0168, wR_p = 0.0216, χ^2 = 1.344						
Element	x	y	z	Occupancy	U_{iso}	Multiplicity
Ca1	−0.006(2)	0.756(9)	0.393(0)	1	0.038(0)	8
Ca2	−0.490(7)	0.51(8)	0.608(9)	1	0.034(9)	8
Fe1	0.439(5)	0.719(2)	0.25	0.5	0.032(3)	4
Co1	0.439(5)	0.719(2)	0.25	0.5	0.032(3))	4
Fe2	−0.054(2)	0.539(3)	0.25	0.5	0.041(7)	4
Co2	−0.054(2)	0.539(3)	0.25	0.5	0.041(7)	4
Fe3	−0.504(0)	0.75	0.5	0.5	0.026(7)	4
Co3	−0.504(0)	0.75	0.5	0.5	0.026(7)	4
Fe4	0.0	0.0	0.0	0.5	0.043(8)	4
Co4	0.0	0.0	0.0	0.5	0.043(8)	4
O1	0.113(7)	0.661(9)	0.25	1	0.045	4
O2	0.604(9)	0.552(4)	0.25	1	0.045	4
O3	−0.212(8)	0.611(3)	0.487(6)	1	0.045	8
O4	−0.761(8)	0.608(6)	0.491(1)	1	0.045	8
O5	0.043(6)	0.458(5)	0.358(4)	1	0.045	8
O6	0.528(6)	0.781(6)	0.365(6)	1	0.045	8

Table 3. Refined structural parameters of $CaSrFeCoO_{6-\delta}$ using powder X-ray diffraction.

Space group: *Ibm*2						
a = 5.5576(3) Å, b = 15.1657(6) Å, c = 5.4141(0) Å, Rp = 0.0165,wRp = 0.0221, χ^2 = 1.830						
Elements	x	y	z	Occupancy	U_{ISO}	Multiplicity
Ca1	0.5102(8)	0.1115(9)	−0.003(5)	0.5	0.023(6)	8
Sr1	0.5102(8)	0.1115(9)	−0.003(5)	0.5	0.023(6)	8
Fe1	0.0776(1)	0.25	−0.011(2)	0.5	0.030(0)	4
Co1	0.0776(1)	0.25	−0.011(2)	0.5	0.030(0)	4
Fe2	0	0	0	0.5	0.032(1)	4
Co2	0	0	0	0.5	0.032(1)	4
O1	0.254(1)	0.0007(8)	0.267(8)	1	0.042(3)	8
O2	−0.074(5)	0.1543(8)	−0.005(2)	1	0.042(3)	8
O3	0.371(7)	0.25	0.852(4)	1	0.042(3)	4

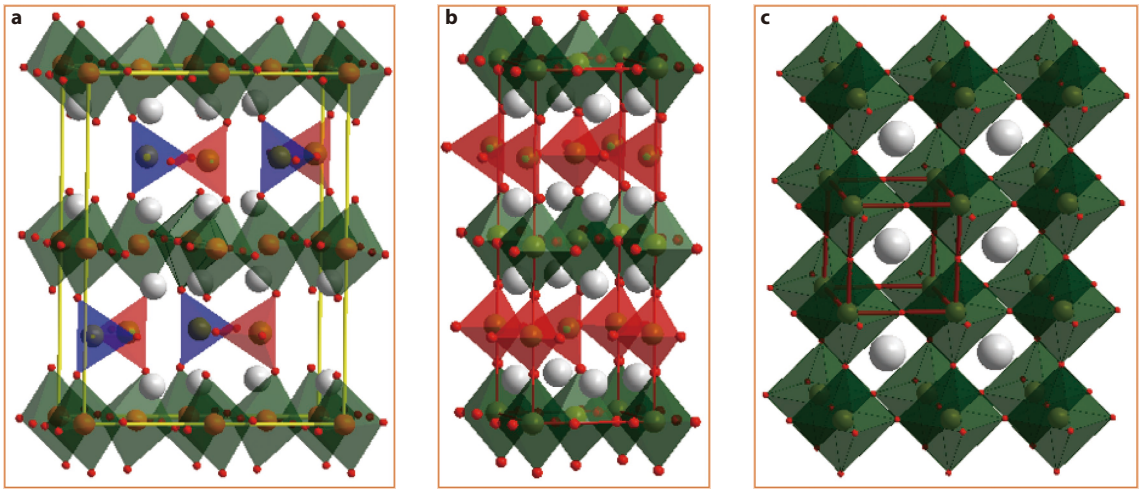


Fig. 2 The crystallographic structures of **a** $Ca_2FeCoO_{6-\delta}$, **b** $CaSrFeCoO_{6-\delta}$, and **c** $Ca_{2/3}Sr_{2/3}Ba_{2/3}FeCoO_{6-\delta}$.

rangement of octahedral layers, tetrahedral chains, and ordered oxygen vacancies gives rise to the orthorhombic symmetry of the brownmillerite structure.[4] Figure (1b) shows the crystal structure of the orthorhombic Ibm2 brownmillerite phase. Similar to the *Pbcm* structure, it consists of alternating layers of BO_6 octahedra (green polyhedra) and BO_4 tetrahedra (red polyhedra), which are formed by the ordered arrangement of oxygen vacancies in the parent perovskite structure. The oxygen vacancies are confined to the tetrahedral layers, where the BO_4 tetrahedra are connected into one-dimensional zigzag chains. Unlike the *Pbcm* structure, however, all the tetrahedral chains in the *Ibm*2 phase have the same orientation (same handedness) throughout the crystal instead of alternating between left- and right-handed

DOI: 10.54227/mlab.20260112

chains. This uniform arrangement of the tetrahedral chains gives rise to the *Ibm*2 space group. The alternating layers of octahedra and uniformly oriented tetrahedral chains define the characteristic crystal structure of the *Ibm*2 brownmillerite phase.[4]

Interestingly, the orthorhombic structure of $CaSrFeCoO_{6-\delta}$ transitions to a cubic structure upon the introduction of Ba, resulting in the compound CSBFC, where the A-site contains equal proportions of Ca, Sr, and Ba. This structural transformation underscores the role of A-site cation size in modulating vacancy ordering and overall crystal symmetry. Notably, all the materials discussed were synthesized under identical conditions, allowing for a direct comparison of their structural characteristics.

A systematic correlation was observed between the A-site cationic radius and the degree of vacancy ordering across the series of compounds. The average ionic radii of the A-site cations increase in the order: $Ca_2FeCoO_{6-\delta}$ (2.68 Å) < $CaSrFeCoO_{6-\delta}$ (2.78 Å) < $Ca_{2/3}Sr_{2/3}Ba_{2/3}FeCoO_{6-\delta}$ (2.941 Å). The radius was calculated based on the Shannon ionic radius.[8] This increase in ionic radius is accompanied by a corresponding decrease in vacancy ordering, with $Ca_2FeCoO_{6-\delta}$ exhibiting the most highly ordered vacancy arrangement and CSBFC showing the least order. This finding highlights how increasing the average A-site cation size leads to a more disordered distribution of oxygen vacancies, transitioning from an ordered brownmillerite structure to a disordered cubic phase. The XRD patterns reveal a gradual change in the average crystal structure from $Ca_2FeCoO_{6-\delta}$ to $Ca_{2/3}Sr_{2/3}Ba_{2/3}FeCoO_{6-\delta}$. The reduced intensity or absence of reflections associated with the brownmillerite superstructure may suggest a decrease in the long-range periodicity of oxygen-vacancy ordering with increasing A-site substitution. However, conventional laboratory XRD is primarily sensitive to the average cation framework and cannot unambiguously determine the local distribution of oxygen vacancies. Therefore, the observed structural changes are interpreted as being consistent with reduced long-range vacancy ordering rather than as direct proof of a specific vacancy arrangement. Additional techniques, such as neutron diffraction, electron diffraction, transmission electron microscopy, or oxygen-content analysis, would be required to determine the vacancy distribution conclusively.

Microstructural analysis

The microstructures of $Ca_2FeCoO_{6-\delta}$, $CaSrFeCoO_{6-\delta}$, and CSBFC were examined using scanning electron microscopy (SEM), as shown in Fig. 3. All three compositions exhibit interconnected polycrystalline microstructures; however, their grain morphology differs significantly. $Ca_2FeCoO_{6-\delta}$ (Fig.3a) consists of relatively large, faceted grains with well-defined grain boundaries, whereas $CaSrFeCoO_{6-\delta}$ (Fig. 3b) exhibits finer, more uniformly distributed grains with a compact microstructure. In contrast, CSBFC (Fig. 3c) shows larger, fused grains accompanied by interconnected pores. The presence of these pores suggests that the material did not achieve complete densification during sintering, despite the apparent grain coalescence. The observed differences in grain morphology and porosity are likely associated with the compositional complexity introduced by the mixed A-site cations (Ca, Sr, and Ba), which can influence diffusion kinetics, grain-boundary mobility, and densification behavior during solid-state sintering. Therefore, the microstructural differences cannot be attributed solely to the larger average A-site ionic radius but are more reasonably related to changes in the sintering behavior caused by A-site substitution. Further quantitative measurements, such as relative density and grain-size analysis, would be required to establish a direct correlation between A-site composition and porosity.

Oxygen stoichiometry and oxidation states

Iodometric titration was employed to determine the oxygen content (δ) in these compounds, revealing values of δ = 1.0 for both $Ca_2FeCoO_{6-\delta}$ and $CaSrFeCoO_{6-\delta}$, while CSBFC exhibited a slightly lower δ value of 0.8. This indicates that the oxidation states of Fe and Co in $Ca_2FeCoO_{6-\delta}$ and $CaSrFeCoO_{6-\delta}$ are predominantly +3, while in CSBFC, a mixed oxidation state of +3 and +4 for Fe and +2 and +3 for Co is suggested. The variation in oxygen content and stoichiometry likely contributes to the observed structural differences, with CSBFC's mixed oxidation states and reduced vacancy ordering potentially enhancing its structural flexibility.

X-ray photoelectron spectroscopy (XPS) measurements were carried out with a monochromatic Al Kα X-ray source ($h\nu$ = 1486.6 eV). The spectra were collected under ultra-high vacuum, and the binding energy scale was calibrated using the adventitious carbon C 1s peak at 284.8 eV. High-resolution spectra were analyzed using CasaXPS, with Gaussian-Lorentzian peak fitting to determine the oxidation states of the constituent elements. X-ray photoelectron spectroscopy (XPS) was performed to determine the surface oxidation states of Fe and Co in CSBFC. The high-resolution Fe 2p and Co 2p spectra are shown in Fig. 4. The Fe $2p_{3/2}$ spectrum (Fig. 4a) ex-

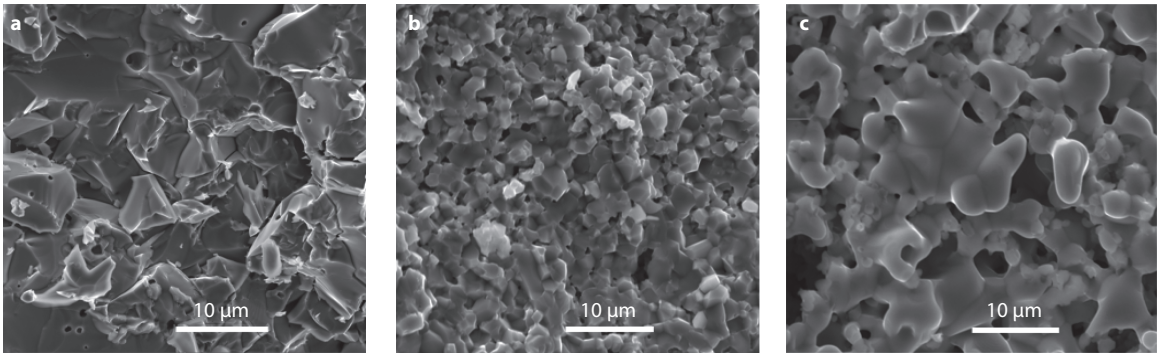


Fig. 3 SEM images of **a** $Ca_2FeCoO_{6-\delta}$, **b** $CaSrFeCoO_{6-\delta}$, and **c** $Ca_{2/3}Sr_{2/3}Ba_{2/3}FeCoO_{6-\delta}$.

DOI: 10.54227/mlab.20260112

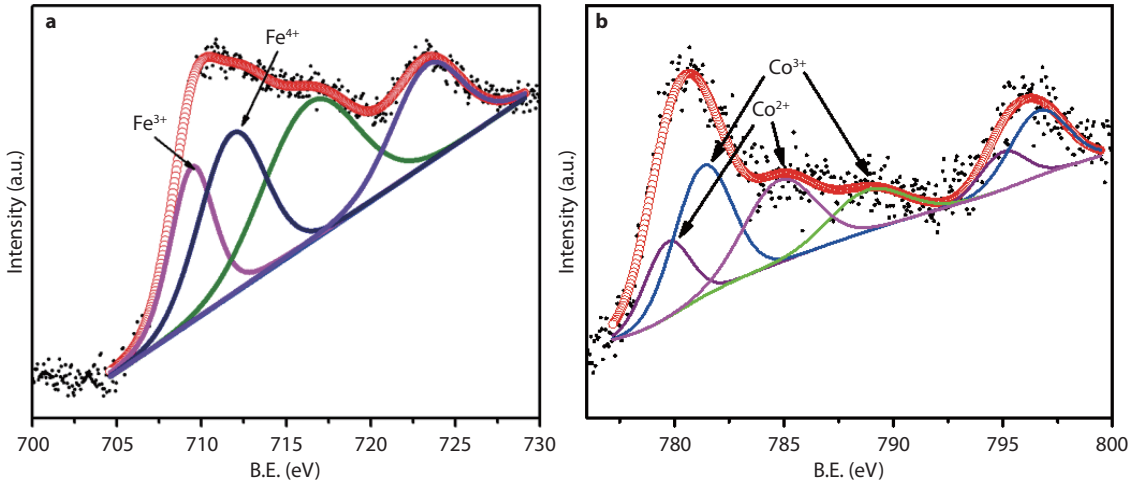


Fig. 4 XPS data of $Ca_{2/3}Sr_{2/3}Ba_{2/3}FeCoO_{6-\delta}$.

hibits peaks centered around 710 eV and higher binding energies, indicating the coexistence of Fe^{3+} and Fe^{4+} oxidation states, consistent with previous reports. Similarly, the Co $2p_{3/2}$ spectrum (Fig. 4b) shows peaks centered around 780 eV and higher binding energies, confirming the presence of mixed Co^{2+} and Co^{3+}oxidation states. The coexistence of multiple oxidation states for both Fe and Co is characteristic of brownmillerite oxides and is associated with charge compensation arising from ordered oxygen vacancies. These oxidation states are also consistent with the synthesis of CSBFC in air using Fe_2O_3 and Co_3O_4 as the starting precursor oxides. [9-12]

Electrical properties analysis

The electrical conductivity of the synthesized materials was measured using the four-probe DC method on as prepared pellets (point connection shown in figure 5), aiming to understand the charge transport characteristics. This method involves applying a constant current or voltage and measuring the corresponding output, allowing for the calculation of total conductivity (σ) using the formula:[13]

$$\sigma = \frac{l}{V} \times \frac{1}{2\pi sF}$$

Where V, S, d, and F are Voltage (V), distance between the probes (cm), diameter of the pellet (cm) and correction factor, respectively. Here, F = t/d, t being the thickness (cm). The 4-probe connection is shown in Fig. 5, applied for conductivity measurements.

To explore the relationship between structural order and electrical conductivity, we measured the conductivity of three compounds: $Ca_2FeCoO_{6-\delta}$, $CaSrFeCoO_{6-\delta}$, and $Ca_{2/3}Sr_{2/3}Ba_{2/3}FeCoO_{6-\delta}$ (CSBFC). The average ionic radius of the A-site cations increases sequentially from $Ca_2FeCoO_{6-\delta}$ to $CaSrFeCoO_{6-\delta}$ to CSBFC, leading to an increase in vacancy disorder. i.e.

$$Ca_2FeCoO_{6-\delta} < CaSrFeCoO_{6-\delta} < Ca_{2/3}Sr_{2/3}Ba_{2/3}FeCoO_{6-\delta}$$

(A-site ionic size increases from left to right. Similarly, the vacancy disorder or structural disorder increases from left to right.)

The conductivity values at 25 °C and 800 °C are tabulated in Table 4. The conductivity is the highest for $Ca_{2/3}Sr_{2/3}Ba_{2/3}FeCoO_{6-\delta}$ thought the measured temperatures (see Fig. 6).

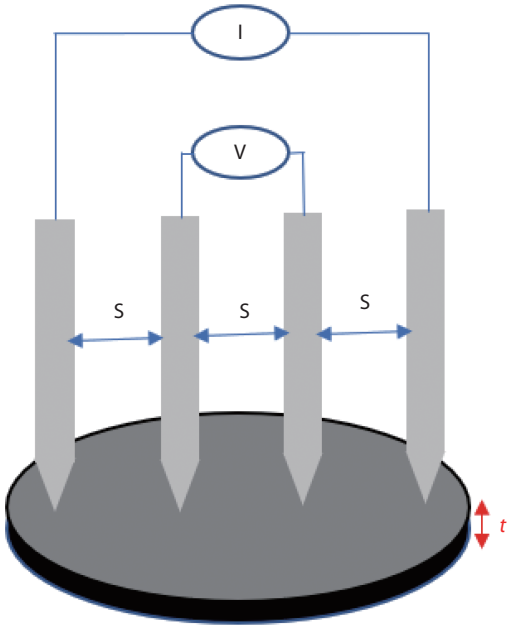


Fig. 5 4-Probe connections to measure charge transport in a pellet.

Here, we can see that the least ordered, CSBFC, has the highest conductivity and the most ordered, $Ca_2FeCoO_{6-\delta}$, has the lowest conductivity. This inverse relationship between structural order and conductivity suggests that materials with higher structural disorder exhibit greater electrical conductivity.

Transition to metallic behavior

A significant observation is the temperature at which these materials transition to metallic-like conductivity. Fig. 6 shows the temperature dependent conductivity of the studied three materials. $Ca_2FeCoO_{6-\delta}$ does not exhibit this transition within the temperature range studied, while $CaSrFeCoO_{6-\delta}$ shows a downturn in conductivity at around 500°C, and CSBFC at approximately 400°C. The earlier onset of metallic behavior in

DOI: 10.54227/mlab.20260112

Table 4. The total (mixed ionic and electronic) conductivity at 25 °C and 800 °C.

compound	total ionic/electronic conductivity at 25 °C (S cm^{-1})	total ionic/electronic conductivity at 800 °C (S cm^{-1})
$Ca_2FeCoO_{6-\delta}$	(6.81±0.15) ×10^{-7}	0.29003 ± 0.008
$CaSrFeCoO_{6-\delta}$	0.00306 ± 0.00010	0.65498 ± 0.014
$Ca_{2/3}Sr_{2/3}Ba_{2/3}FeCoO_{6-\delta}$	0.01027 ± 0.00021	1.2658 ± 0.021

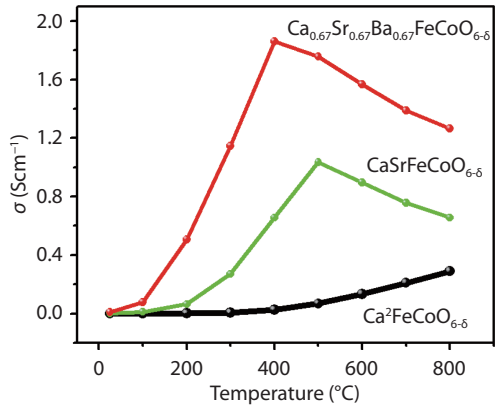


Fig. 6 Temperature dependent mixed electronic/ionic conductivity of $Ca_2FeCoO_{6-\delta}$ (black) and $CaSrFeCoO_{6-\delta}$ (green), and $Ca_{2/3}Sr_{2/3}Ba_{2/3}FeCoO_{6-\delta}$ (red).

CSBFC corresponds to its high vacancy disorder. This phenomenon suggests that greater structural disorder lowers the transition temperature, hinting at a correlation between vacancy distribution and the metallic transition.

Charge transport mechanism

In ODPs, electrical conductivity typically arises from multiple oxidation states of the B-site cations (e.g., Fe^{3+}/Fe^{4+} and Co^{2+}/Co^{3+}). Charge transport occurs via electron hopping through metal–oxygen-metal M^{m+}- O^{2-}- M^{n+} bonds. For our materials, this mechanism is facilitated by the overlap between Fe/Co-3d orbitals and oxygen 2p orbitals, resulting in electron hopping through Fe^{3+}/Co^{2+}–O^{2-}–Fe^{4+}/Co^{3+} pathways. Thus, the concentration of these pathways significantly influences the overall charge transport. The iodometric titration results indicate that δ values are 1 for $Ca_2FeCoO_{6-\delta}$ and $CaSrFeCoO_{6-\delta}$, implying all Fe and Co are in the +3-oxidation state. Meanwhile, CSBFC shows a δ value of 0.8, corresponding to mixed oxidation states (+3 and +4) for Fe and (+2 and +3) for Co. XPS data also show similar results. Consequently, CSBFC has a higher concentration of conduction pathways, leading to enhanced electrical conductivity.

Impact of structural distortions on conductivity

The bond angles within the crystal lattice play a crucial role in determining the conductivity of these materials. The Rietveld refinement result shows that the bond angle of Fe/Co–O–Fe/Co is nearly ideal (180°) in CSBFC, while $CaSrFeCoO_{6-\delta}$ and $Ca_2FeCoO_{6-\delta}$ exhibit smaller bond angles of 165.4° and 163.5°, respectively. Smaller bond angles arise from structural distortions that reduce electron mobility due to lattice polarization, promoting polaronic charge transport. The larger bond angle in $CaSrFeCoO_{6-\delta}$ contributes to its relatively higher conductivity compared to $Ca_2FeCoO_{6-\delta}$.

It has been demonstrated through density functional theory (DFT) for other similar materials that when the Co–O–Co bond angles approach 180° (as seen in doped $La_{1-x}Sr_xCoO_3$ systems), the overlap between the unoccupied Co-3d conduction band and the occupied O-2p valence band increases, enhancing conductivity. Similar trends are seen in our materials, where increasing the A-site cation size reduces bond distortions, thus, increasing bond angles and improving conductivity.

Temperature-dependent conductivity

The variable-temperature conductivity measurements of $Ca_2FeCoO_{6-\delta}$, $CaSrFeCoO_{6-\delta}$, and CSBFC are shown in Fig. 6. All three materials display semiconducting behavior with conductivity increasing with temperature, which is typical for ODPs due to the thermally activated mobility of charge carriers (polarons). The relation governing this behavior is:

$$\sigma = ne\mu$$

where σ is the conductivity, n is the carrier concentration, e is the charge, and $\mu$is the mobility of charge carriers. The semiconducting ODPs studied here exhibit p-type behavior, where electron holes serve as the primary charge carriers.[14-16]

Interestingly, $CaSrFeCoO_{6-\delta}$ and CSBFC show a semiconductor-to-metal transition at elevated temperatures, likely due to an increase in polaron mobility followed by a limit where phonon-carrier scattering dominates, reducing conductivity.[17] This transition aligns with the observed oxygen content variation, where oxygen-deficient pathways Fe^{3+}/Co^{3+}–O^{2-}–Fe^{4+}/Co^{4+} are disrupted, potentially due to oxygen loss at higher temperatures.

These observations suggest that the introduction of larger A-site cations (like Ba) increases both the disorder and conductivity, driving the materials closer to metallic-type behavior while retaining semiconducting properties at lower temperatures. The findings highlight the intricate balance between structural order, vacancy arrangement, and electronic properties in oxygen-deficient perovskite materials.

Conclusion

In conclusion, this study demonstrates that systematic A-site cation engineering is an effective strategy for controlling structural symmetry, vacancy ordering, and charge transport in oxygen-deficient perovskites. By increasing the average A-site ionic radius from $Ca_2FeCoO_{6-\delta}$ to $CaSrFeCoO_{6-\delta}$ and finally to $Ca_{2/3}Sr_{2/3}Ba_{2/3}FeCoO_{6-\delta}$, a clear structural evolution from an ordered brownmillerite phase to a disordered cubic perovskite was achieved under identical synthesis conditions. This progressive reduction in vacancy ordering is directly correlated with enhanced electrical conductivity, earlier onset of metallic-like behavior, and increased structural symmetry in CSBFC. The cubic CSBFC phase benefits from near-ideal Fe/Co–O–Fe/Co bond angles, mixed valence states of Fe and Co, and higher oxygen-vacancy disorder, all of which collectively facilitate improved charge transport. These results establish a direct link between A-site cation size, vacancy disorder, and electronic properties, highlighting the structural

DOI: 10.54227/mlab.20260112

flexibility of oxygen-deficient perovskites. The insights gained from this work provide a rational framework for designing perovskite oxides with tailored electrical properties, making them promising candidates for applications in catalysis, solid oxide fuel cells, and other energy-related technologies.

■ INSTITUTIONAL REVIEW BOARD STATEMENT

Not Applicable

■ INFORMED CONSENT STATEMENT

Not applicable

■ ACKNOWLEDGMENTS

This work is partly supported by the NSF TCUP Tribal Enterprise Advancement Center supports a part of this work, grant no. HRD 1839895. A part of the work is supported by National Aeronautics and Space Administration (NASA) Award No. 80NSSC24M0025. Additional support for the work came from ND EPSCOR STEM equipment grants.

■ CONFLICTS OF INTEREST

The authors declare no conflict of interest.

■ REFERENCES

1. R. K. Hona, F. Ramezanipour, *Angew. Chem. Int. Ed.*, 2019, 58, 2060
2. J. H. Kim, A. Manthiram, *J. Mater. Chem. A*, 2015, 3, 24195
3. R. K. Hona, A. Huq, S. Mulmi, F. Ramezanipour, *Inorg. Chem.*, 2017, 56, 9716
4. R. K. Hona, A. Huq, F. Ramezanipour, *Inorg. Chem.*, 2017, 56, 14494
5. A. C. Larson, A. C. Von Dreele, *Los Alamos National Laboratory Report LAUR*, 1994, 86 - 748.
6. B. H. Toby, *J. Appl. Crystallogr.*, 2001, 34, 210
7. R. K. Hona, G. S. Dhaliwal, R. Thapa, *Appl. Sci.*, 2022, 12, 2930
8. R. D. Shannon, C. T. Prewitt, *Acta Crystallogr. B*, 1969, 25, 925
9. J. Li, Z. Li, F. Ning, L. Zhou, R. Zhang, M. Shao, M. Wei, *ACS Omega*, 2018, 3, 1675
10. A. Subedi, D. Yang, W. K. Chin, B. Tamang, S.Sahoo, P. Yancey, R. Mahbub, J. Shield, R. Y. Lai, X. Xu, P. A. Dowben,V. Rangari , *J. Condens. Matter Phys.*, 2024, 36, 285001
11. M. Ghaffari, T. Liu, H. Huang, O. K. Tan, M. Shannon, *Mater. Chem. Phys.*, 2012, 136, 347
12. C. Ruttanapun, S. Maensiri, *J. Phys. D: Appl. Phys.*, 2015, 48, 495103
13. L. Sun, S. S. Park, D. Sheberla, M. Dincă, *J. Am. Chem. Soc.*, 2016, 138, 14772
14. P. Ren, N. Masó, Y. Liu, L. Ma, H. Fan, A. R. West, *J. Mater. Chem. C*, 2013, 1, 2426
15. P. Ren, N. Masó, A. R. West, *Phys. Chem. Chem. Phys.*, 2013, 15, 20943
16. A. L. Shaula, V. V. Kharton, M. V. Patrakeev, J. C. Waerenborgh, D. P. Rojas, F. M. B. Marques, *Ionics*, 2004, 10, 378
17. H. -C. Yu, K. -Z. Fung, *J. Mater. Res.*, 2004, 19, 943

©2026 The Authors. *Materials Lab* is published by Lab Academic Press. This is an open access article under the terms of the Creative Commons Attribution License, which permits use, distribution and reproduction in any medium, provided the original work is properly cited.